Experimental Demonstration of LLO Continuous-Variable Quantum Key Distribution With Polarization Loss Compensation

Tao Shen, Xiangyu Wang, Ziyang Chen, Huiping Tian, *Member, IEEE*, Song Yu, and Hong Guo, *Member, IEEE*

***Abstract*—The compensation process for the state of polarization (SOP) from quantum signal plays an important role in the practical implementation of continuous-variable quantum key distribution (CV-QKD). In contrast to the previous scheme using an expensive digital dynamic polarization controller, we choose a cheaper manual polarization controller interfaced with a digital algorithm based on Kalman filter to achieve compensation of the polarization loss under the condition that the SOP of the fiber is relatively stable. This paper also enumerates the details of other digital signal processing method to achieve final secret key rate. And a pilot-sequential Gaussian modulated coherent state (GMCS) continuous-variable quantum key distribution system with a local local oscillator (LLO) is experimentally implemented based on the analysis of excess noise. Finally, the experimental results show that the method of polarization loss compensation takes advantages in maintaining the stability of the final secret key rate. And a secret key rate of 110 kbps is achieved within 20 km optical fiber (with 4 dB loss) under the finite-size block of 1×10^6 during a more extended time in the laboratory.**

***Index Terms*—State of polarization, continuous-variable quantum key distribution, pilot-sequential, Kalman filter, digital signal processing.**

I. Introduction

CONTINUOUS-VARIABLE quantum key distribution (CV-QKD) allows two authenticated participants, referred to as Alice and Bob, to establish secure symmetric keys through an untrusted channel using quadratures components of quantum states [1], [2]. Up to now, the security of CV-QKD protocols has been well proved, mainly including the security against collective attacks [3], [4], [5] and coherent attacks [6], [7]. Moreover, the security for some protocols, such as Gaussian modulated coherent state (GMCS) heterodyne protocol, have been completely proved under the universal framework of composable security [8], [9], [10]. GMCS protocol is also the most widely used protocol because the preparation and reception of quantum states can be realized entirely by commercial optical devices such as lasers, optical modulators, and balanced homodyne detectors [11], [12]. In addition, there are also important theories and implementations in the application of networking [13], [14]. In the GMCS CV-QKD scheme, there are two types of systems named by transmitting local oscillator (TLO) and local local oscillator (LLO) for whether Alice sends the local oscillator (LO) signal to Bob. The advantage of the TLO is that the local oscillator and the modulation signal come from the same laser, and Bob can directly acquire the baseband modulation signal without complex digital signal processing from the coherent detection. Thus the secret key rate can be obtained in real time in the practical implementation of CV-QKD [15], [16], [17], [18].

However, the TLO system also suffers from many problems: photon leakage from the LO, shot noise can not reach its limit resulting from channel attenuation, and could not prevent attacks on the LO from Eve. By contrast, the LLO system can effectively solve the above problems. Recently, there have been many experimental implementations of LLO systems, both inside and outside the laboratory [14], [19], [20]. However, it is more difficult to recover the quantum signal compared with TLO systems, and introducing additional pilot signal is a great method in this way. The multiplexing of the pilot signal in the LLO system is a key issue affecting the system performance, and has been analyzed respectively [21]. According to the multiplexing method, the LLO system contains pilot-sequential LLO system [22] and pilot-multiplexed LLO system referred to as time division multiplexing (TDM) and frequency division multiplexing (FDM) [23], [24]. The pilot-sequential LLO system has the advantage of zero photon leakage from pilot signals compared with the pilot-multiplexed LLO system under the analysis of excess noise [21].

Manuscript received 20 November 2022; revised 7 February 2023; accepted 15 February 2023. Date of publication 20 February 2023; date of current version 27 February 2023. This work was supported in part by the Key Program of National Natural Science Foundation of China under Grant 61531003, in part by the National Natural Science Foundation of China under Grants 62001041 and 62201012, in part by the Fundamental Research Funds of BUPT under Grant 2022RC08, and in part by the Fund of State Key Laboratory of Information Photonics and Optical Communications under Grant IPOC2022ZT09. *(Corresponding authors: Xiangyu Wang; Ziyang Chen.)*

Tao Shen and Huiping Tian are with the State Key Laboratory of Information Photonics and Optical Communications, Beijing University of Posts and Telecommunications, Beijing 100876, China, and also with the School of Information and Communication Engineering, Beijing University of Posts and Telecommunications, Beijing 100876, China (e-mail: 704648404@qq.com; hptian@bupt.edu.cn).

Xiangyu Wang and Song Yu are with the State Key Laboratory of Information Photonics and Optical Communications, Beijing University of Posts and Telecommunications, Beijing 100876, China (e-mail: xywang@bupt.edu.cn; yusong@bupt.edu.cn).

Ziyang Chen and Hong Guo are with the State Key Laboratory of Advanced Optical Communication Systems and Networks, School of Electronics, and Center for Quantum Information Technology, Peking University, Beijing 100871, China (e-mail: chenziyang@pku.edu.cn; hongguo@pku.edu.cn).

Digital Object Identifier 10.1109/JPHOT.2023.3246500

Herein, we propose a pilot-sequential LLO experimental system based on GMCS heterodyne protocol. In order to simplify the system, we adopt some improvements to the optical layout. At the Alice's side, an additional amplitude modulator is applied in the state preparation to maximize the the signal to ratio (SNR) of the pilot signal [18]. At the Bob's side, heterodyne detection can be accomplished using only one balanced homodyne detector (BHD). And the quadrature components X and P can be obtained by Bob at the same time from digital method instead of the traditional 90° optical hybrid [25], [26], which can effectively eliminate the influence of measurement angular error from the imperfection of devices [27]. Furthermore, we use a manual polarization controller (MPC) to replace the expensive digital dynamic polarization controller (DPC). It is worth noting that the experiment is conducted on the premise that the SOP of fiber is stable respectively and can be controlled by the MPC within a certain range. This is because both buried and laboratory fibers have their own rotation coefficients of SOP which are fixed, and the SOP does not change drastically with relatively small external perturbations.

In order to eliminate the remaining polarization loss caused by MPC's instability this paper utilizes a digital algorithm based on the Kalman filter (KF). It is worth mentioning that the compensation algorithm is to compensate the loss from SOP rather than replacing the MPC. The KF algorithm conducts closed-loop management on errors by using observation data and estimated data and limits the mistakes to a specific range, which can efficiently reduce some noise caused by observation deviation or calculation deviation. Therefore, the KF algorithm has been widely used in classical communication systems [28], and even in CV-QKD systems in recent years [29], [30], [31]. Additionally, compared to the work of tracking SOP with KF at different rotation factors from fibre [29], our work aims to emphasize the importance of polarization loss compensation (PLC) even under conditions that the SOP changes slowly. The pilot-sequential system is a single polarization system, and the polarization loss of the pilot signal is equivalent to the quantum signal within a pulse cycle based on the above assumption. SOP's jitter directly causes the quantum signal's attenuation at single polarization, which is equivalent to channel attenuation in a single polarization system, so it can be considered a linear process. Digital signal processing (DSP) method plays a vital importance on current LLO systems, in addition to traditional data post-processing [32], [33], [34], DSP algorithms for recovering quantum signals have received extensive attention [31], [35], [36] and new analysis methodology is proposed recently [37]. Thus, in addition to KF, we also list other digital data processing method to achieve final secret key rate. By using the above method, we can get a stable secret key rate of 110 kbps with high robustness under the finite-size block of $N = 1 \times 10^6$ with a low level of excess noise of about 0.02 at the transmission distance of 20 km over a long period of time of 8 hours.

The paper is organized as follows. In Section II, we provide a concrete pilot-sequential LLO experimental system based on GMCS heterodyne protocol. In Section III, we will discuss details of four DSP steps concretely by sequence, including frequency estimation, orthogonal components acquiring, polarization loss compensation, and phase compensation. Then in Section IV, system performance and discussion in practical implementation are provided. The paper is concluded In Section V.

II. Experimental Setup

We perform an implementation of pilot-sequential LLO GMCS CV-QKD based on heterodyne protocol. The experimental setup is depicted in Fig. 1. At Alice's side, the continuous-wave coherent light is generated by a frequency-stabilized laser at 1550.12 nm with a lower phase noise of $-130\ dB@100\,\text{Hz}$ than $-110\ dB@100\,\text{Hz}$ used in [18]. Then, an acoustic-optic modulator (AOM) is used to generate optical pulses at a repetition rate of 5 MHz with a high extinction rate of 60 dB. The optical pulses are then modulated by an amplitude modulator with Rayleigh distribution and a phase modulator with uniform distribution to get a Gaussian modulation. Note that the quantum signals need to be pulsed signals instead of continuous signals for more precisely extracting the heterodyne-detected products with better signal-to-noise ratio (SNR) in practical experiment. And the duration of the quantum signal is determined to be 80 ns in the case of the generated square wave signal with repetition frequency of 5 MHz. The second amplitude modulator is used to improve the SNR of the pilot signal to enhance the accuracy of phase compensation [18], which is analyzed in Appendix. B. In addition, it also provides a way to attenuate the quantum signal with an optimal modulation variance V_A around 4 in this paper. so an amplitude modulator with practical extinction rate of 40 dB is required as well as a variable optical attenuator (VOA). And this is the best way to acquire the optimal modulation variance. Note that if the modulator extinction ratio is too large such as 60 dB, the quantum signal will be too small (modulation variance less than 0.1) to be detected at the receiver. In particular, we use a bias controller to control the amplitude modulator's bias dynamically, ensuring the long-term stability of the modulation variance and void imperfect state preparation [38]. The pulse modulation electrical signals and the Gaussian modulation electrical signals are all generated by FPGA and the self-developed digital-to-analog converter (DAC) with a resolution ratio of eight bits. Our experiment uses a 20 km fiber spool with an attenuation coefficient of 0.2 dB/km as a quantum channel. At Bob's side, the MPC is used to maintain the optimal polarization state of the signal to improve the signal quality as high as possible. Meanwhile, the LO is produced by another frequency-stabilized laser at 1550.12 nm. The optical power of the LO is required high, 10.3 dBm in our experiment, to meet the shot-noise-limited detection of the quantum signals. The beam splitter (BS) with a fast axis cut-off ensures stable interference between the signal and the LO at a single polarization direction. Two VOAs with the same length are employed to adjust the output of the BS, followed by a self-developed BHD with a bandwidth of 350 MHz. Note that the frequency offset between the laser at the transmitter and the laser at the receiver should be controlled by Bob within a reasonable range, which is about 200 MHz in our experiment. On the one hand, it

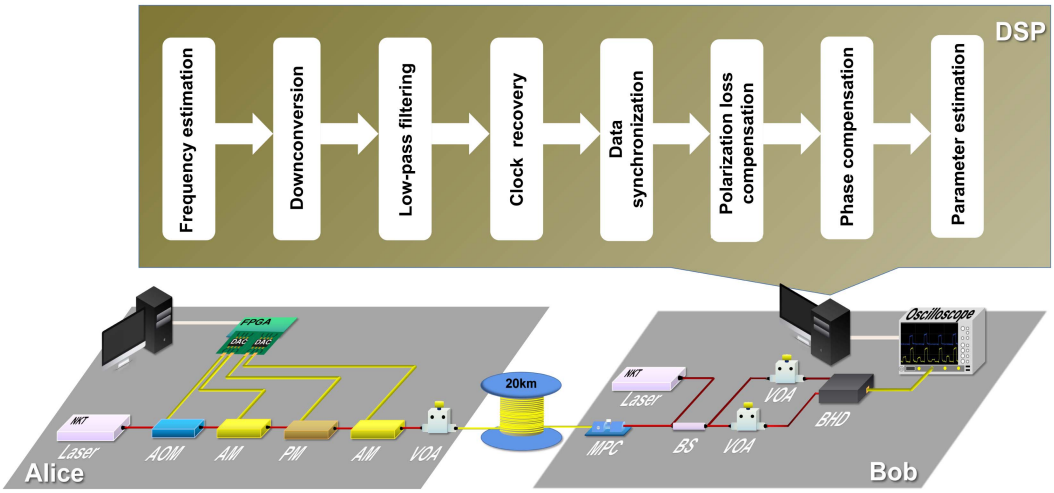

Fig. 1. Optical layout and DSP routine of the GMCS protocol with heterodyne detection. AOM: acoustic-optic modulator; AM: amplitude modulator; PM: phase modulator; VOA: variable optical attenuator; MPC: manual polarization controller; BS: beam splitter; BHD: balanced homodyne detector; DSP: digital signal processing.

eliminates the low-frequency noise; on the other hand, the signal can be completely detected. At last, the detected analog signals are sampled by an oscilloscope with 500 MSa/s and uploaded to a computer with high performance.

III. Digital Signal Processing

A. Frequency Estimation

Before digital signal processing, we first need to analyze the expressions of the sampled signals. The electric field expressions of the signal and the LO before detection can be expressed by [39]

$$E_{\mathrm{sig}} = TT_{\mathrm{P}} A_{\mathrm{sig}} \cos\left(2\pi(f_{\mathrm{A}}+\Delta f_{\mathrm{A}})t+\phi_{\mathrm{sig}}+\varphi_{\mathrm{sig}}+\varphi_{\mathrm{channel}}^{\mathrm{sig}}\right), \tag{1}$$

$$E_{\mathrm{ref}} = TT_{\mathrm{P}} A_{\mathrm{ref}} \cos\left(2\pi(f_{\mathrm{A}}+\Delta f_{\mathrm{A}})t+\varphi_{\mathrm{ref}}+\varphi_{\mathrm{channel}}^{\mathrm{ref}}\right), \tag{2}$$

$$E_{\mathrm{LO_{sig}}} = A_{\mathrm{LO_{sig}}} \cos\left(2\pi(f_{\mathrm{B}}+\Delta f_{\mathrm{B}})t+\varphi_{\mathrm{LO_{sig}}}\right), \tag{3}$$

$$E_{\mathrm{LO_{ref}}} = A_{\mathrm{LO_{ref}}} \cos\left(2\pi(f_{\mathrm{B}}+\Delta f_{\mathrm{B}})t+\varphi_{\mathrm{LO_{ref}}}\right), \tag{4}$$

where E_{sig} and E_{ref} represent electric field intensity of the quantum signal and the pilot signal respectively, $E_{\mathrm{LO_{sig}}}$ and $E_{\mathrm{LO_{ref}}}$ represent the electric field intensity of the LO corresponding to the quantum signal and the pilot signal. T denotes the transmittance of the quantum channel while T_{P} represents the polarization loss from imperfect MPC. And we assume that the adjacent pilot signal and quantum signal are subject to the same polarization loss T_P within a pulse cycle. The modulated amplitude A_{sig} and phase ϕ_{sig} follow the Rayleigh distribution and the uniform distribution. φ_{sig}, φ_{ref}, $\varphi_{\mathrm{LO_{sig}}}$, $\varphi_{\mathrm{LO_{ref}}}$ represent initial phase of the laser from different moments. $\varphi_{\mathrm{channel}}^{\mathrm{sig}}$ and $\varphi_{\mathrm{channel}}^{\mathrm{ref}}$ is defined as the accumulated phase of the signal as it travels through the channel [21], in which $\varphi_{\mathrm{channel}}^{\mathrm{sig}} \approx \varphi_{\mathrm{channel}}^{\mathrm{ref}}$ in this scheme. A_{LO} is the amplitude of the LO and $A_{\mathrm{LO_{ref}}} = A_{\mathrm{LO_{ref}}}$. Since there will be a frequency drift in the laser, we can denote the center frequency of the laser as $f + \Delta f$. After intermediate frequency heterodyne detection, the generated photocurrents can be expressed as respectively

$$\begin{aligned} I_{\mathrm{sig}} &= R\eta\left(\left|E_{\mathrm{sig}}+E_{\mathrm{LO_{sig}}}\right|^2-\left|E_{\mathrm{sig}}-E_{\mathrm{LO_{sig}}}\right|^2\right) \\ &= 2R\eta TT_{\mathrm{P}} A_{\mathrm{sig}} A_{\mathrm{LO_{sig}}} \cos\left(2\pi\Delta f_{\mathrm{AB}}t+\phi_{\mathrm{sig}}\right. \\ &\quad \left.+\varphi_{\mathrm{fast}}+\varphi_{\mathrm{slow}}^{\mathrm{sig}}\right), \end{aligned} \tag{5}$$

$$\begin{aligned} I_{\mathrm{ref}} &= R\eta\left(\left|E_{\mathrm{ref}}+E_{\mathrm{LO_{ref}}}\right|^2-\left|E_{\mathrm{ref}}-E_{\mathrm{LO_{ref}}}\right|^2\right) \\ &= 2R\eta TT_{\mathrm{P}} A_{\mathrm{ref}} A_{\mathrm{LO_{ref}}} \cos\left(2\pi\Delta f_{\mathrm{AB}}t+\varphi_{\mathrm{fast}}+\varphi_{\mathrm{slow}}^{\mathrm{ref}}\right), \end{aligned} \tag{6}$$

where R and η denote the responsiveness and quantum efficiency of the BHD, and $\Delta f_{\mathrm{AB}} = f_{\mathrm{A}} - f_{\mathrm{B}}$ is the frequency difference between two independent lasers. φ_{fast} stem from frequency offset, which changes rapidly. $\varphi_{\mathrm{slow}}^{\mathrm{sig}}$ and $\varphi_{\mathrm{slow}}^{\mathrm{ref}}$ represent initial phase differences at different moments and stay constant within a short interval of time, such as ns. It is worth noting that $\varphi_{\mathrm{slow}}^{\mathrm{sig}} \neq \varphi_{\mathrm{slow}}^{\mathrm{ref}}$.

As seen from the (5), (6), the center frequency of the signal Δf_{AB} is not zero, which is around 200 MHz in our experiment. Therefore, to obtain the baseband signal for subsequent data processing, a fast Fourier transform (FFT) should be performed on the sampled signal first in our experiment. Then the peak frequency of the spectrum would be obtained, which we call frequency estimation. Fig. 2(a) shows BHD's output at frequency domain while Fig. 2(b) shows sampled data at time domain. It is noteworthy that the duration of the signal pulses is 0.2 s in our experiment due to the repetition frequency of 5 MHz and the total block size of 1×10^6, despite a time scale of 1000 us only shown in Fig. 2(a). From Fig. 2(a), we can see that the peak at every repetition frequency of 2.5 MHz is presented in

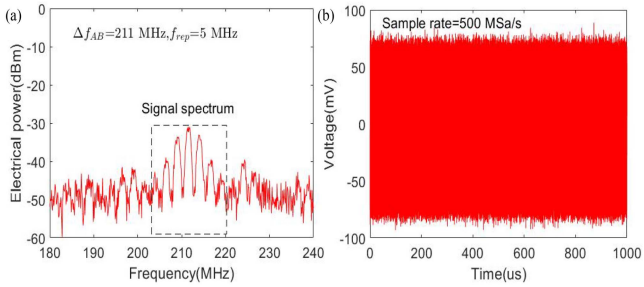

Fig. 2. Heterodyne-detected products of the signal. (a) Frequency spectrum of the output signal. (b) The output signal in the time domain.

the frequency spectrum of the signal, mainly the pilot signal, because the quantum signal is too small to be detected.

B. Orthogonal Components Acquiring

To acquire the frequency spectrum of the baseband signal, the process of orthogonal components acquiring is indispensable, which can be divided into three steps: Downconversion, Low-pass filtering, and Synchronization, and can be written through the following equation [24]:

$$\begin{aligned} X_{\mathrm{sig}} &= LPF\left(real\left(I_{\mathrm{sig}} \cdot e^{-2\pi\Delta f t}\right)\right) \\ &= R\eta T T_{\mathrm{P}} A_{\mathrm{LO_{sig}}} A_{\mathrm{sig}} \cos\left(\phi_{\mathrm{sig}} + \varphi_{\mathrm{fast}} + \varphi_{\mathrm{slow}}^{\mathrm{sig}}\right), \end{aligned} \tag{7}$$

$$\begin{aligned} P_{\mathrm{sig}} &= LPF\left(image\left(I_{\mathrm{sig}} \cdot e^{-2\pi\Delta f t}\right)\right) \\ &= -R\eta T T_{\mathrm{P}} A_{\mathrm{LO_{sig}}} A_{\mathrm{sig}} \sin\left(\phi_{\mathrm{sig}} + \varphi_{\mathrm{fast}} + \varphi_{\mathrm{slow}}^{\mathrm{sig}}\right), \end{aligned} \tag{8}$$

$$\begin{aligned} X_{\mathrm{ref}} &= LPF\left(real\left(I_{\mathrm{ref}} \cdot e^{-2\pi\Delta f t}\right)\right) \\ &= R\eta T T_{\mathrm{P}} A_{\mathrm{LO_{ref}}} A_{\mathrm{ref}} \cos\left(\varphi_{\mathrm{fast}} + \varphi_{\mathrm{slow}}^{\mathrm{ref}}\right), \end{aligned} \tag{9}$$

$$\begin{aligned} P_{\mathrm{ref}} &= LPF\left(image\left(I_{\mathrm{ref}} \cdot e^{-2\pi\Delta f t}\right)\right) \\ &= -R\eta T T_{\mathrm{P}} A_{\mathrm{LO_{ref}}} A_{\mathrm{ref}} \sin\left(\varphi_{\mathrm{fast}} + \varphi_{\mathrm{slow}}^{\mathrm{ref}}\right), \end{aligned} \tag{10}$$

where $LPF(\cdot)$ represent the function of low-pass filtering, $real(\cdot)$ denote the function to obtain the real part X of orthogonal components while $image(\cdot)$ denote the function to obtain the imaginary part P of orthogonal components. Δf is the estimated frequency in Section III-A. We can get orthogonal components from (7)–(10) from ideal DSP rather than conventional optical devices. In other words, this method can effectively eliminate the measurement angular error from the measurement device. Synchronization contains clock recovery and data synchronization. In our experiment, the transmitter and receiver are triggered by the same synchronous source to achieve clock synchronization at the transmitter and receiver for simplicity. Since the repetition rate of the system is 5 MHz, the instability of clock frequency has less influence on the design and could be ignored here. Moreover, some marking signals are embedded in quantum signals for further data synchronization. Finally, we calculate the peak of the pulse in the time domain divided by 100 points as the raw data.

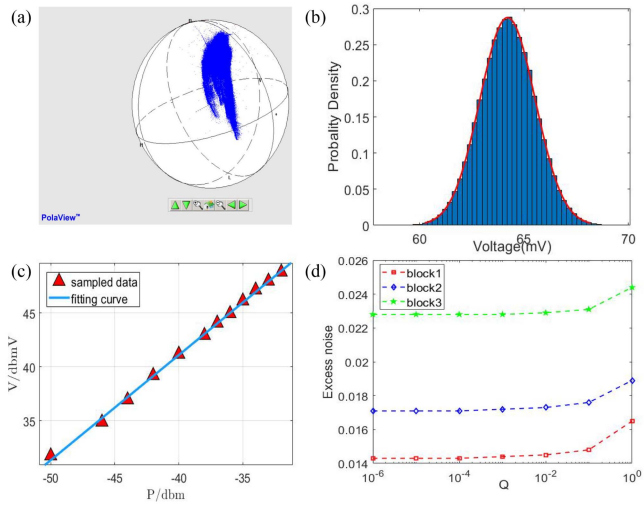

Fig. 3. (a) Six hours SOP test with MPC. (b) The fitted distribution from the amplitude of pilot pulse. (c) Mean value of the amplitude of the measured pilot pulse versus input optical signal power without MPC. (d) The excess noise versus different Q with three blocks data.

C. Polarization Loss Compensation

In this section, we will first introduce the necessity of PLC, as seen in Fig. 3(a). The drift of SOP controlled by MPC is relatively large during six hours which inevitably deteriorates the performance of the practical systems. As we all know, the pilot signal's amplitude is proportional to the channel loss from AWGN channel assumption, and we have denoted the polarization loss T_{P} the attenuation from MPC in (1). So the correlation between the pilot signal and the polarization loss could be obtained:

$$X' = T_{\mathrm{P}} X + N, \tag{11}$$

$$P' = T_{\mathrm{P}} P + N, \tag{12}$$

where $X(P)$ represents the signal before MPC while $X'(P')$ is the signal after MPC, and N is the noise consists mainly from shot noise and electrical noise.

Thus, as long as we estimate the value of ${T_{\mathrm{P}}}^{-1}$ in real time, we can obtain the decay-stabilized quantum signal. According to the sampled data points, we can calculate the expression of the pilot signal's amplitude. From the Fig. 3(b), we can conclude that the amplitude obeys a Gaussian distribution and the amplitude can be written as

$$A' = \frac{T_{\mathrm{P}} \cdot X + N}{\cos(\arctan\frac{T_{\mathrm{P}} \cdot P + N}{T_{\mathrm{P}} \cdot X + N})} \approx T_{\mathrm{P}} \cdot A + N,' \tag{13}$$

where A' is the calculated amplitude of the pilot signal, A is the true amplitude of the pilot signal, $X = A\cos\theta$ and $P = A\sin\theta$ are true quadrature components of pilot signal, N' is the new additive noise. Based on statistical theory, We need to find the average amplitude A of the pilot signal without polarization loss, then we can track it by KF (in Appendix A). It is noted that the change of SOP is a slow-varying process which we assume in this paper, and We can compensate it by each block of data respectively.

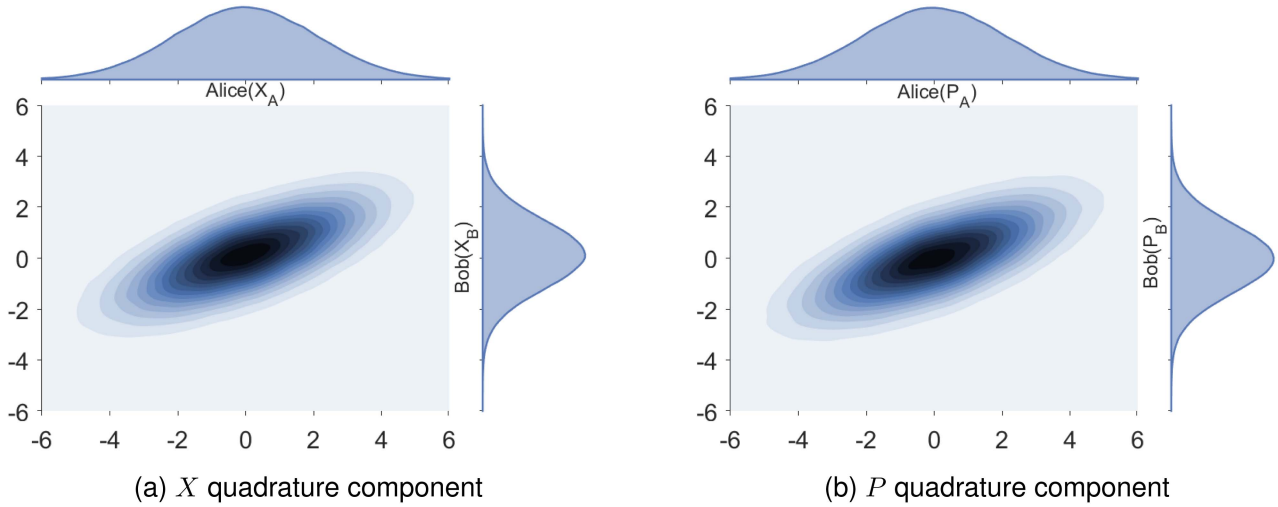

Fig. 4. The correlation of the measured both quadrature components in shot noise between Alice and Bob after phase compensation.

To get the value of A, We need to do confirmatory experiments before the experiment of this scheme. Firstly, a polarization-maintaining VOA is used as the quantum channel, then the correlation between the pilot signal's amplitude and the channel loss could be obtained, as shown in Fig. 3(c). It is worth noting that the dispersion and nonlinear effects of the fiber are so small that they can be ignored in systems with low repetition rates and optical power. Secondly, the optical fiber and MPC are reconnected to measure the channel attenuation, and then the true amplitude of pilot signal under 20 km fiber can be obtained as $U_{\mathrm{o}}(k)$ in Appendix A according to the fitting curve under the condition that the channel attenuation is known. Finally, we achieve the optimal estimation by selecting the appropriate Q and R (R could be calculated by observation data which is about 4×10^{-4}). We evaluate the excess noise for different data blocks with different Q and find that the minimum is reached when Q is less than 10^{-4}, as shown in Fig. 3(d).

D. Phase Compensation

After polarization compensation, the phase compensation of the whole block is proposed. From the (7)–(10), we know that the phase to be compensated contains fast-drift phase φ_{fast} from frequency drift of the laser and slow-drift phase φ_{slow} from laser phase drift between a short time interval. In this scheme, each quantum signal pulse is accompanied by a pilot pulse tracking its phase drift of itself. Thus, one can use the quadrature components of the pilot pulse to calculate each phase [25]:

$$\theta = -\tan^{-1}\left(\frac{P_{\mathrm{R}}}{X_{\mathrm{R}}}\right). \tag{14}$$

By using a relatively strong pilot pulse, Bob can acquire an accurate estimation of θ and use this phase information to implement the compensation of the fast-drift phase by the following equation [40]:

$$\begin{pmatrix} X'_{\mathrm{sig}} \\ P'_{\mathrm{sig}} \end{pmatrix} = \begin{pmatrix} \cos\theta & -\sin\theta \\ -\sin\theta & -\cos\theta \end{pmatrix} \begin{pmatrix} X_{\mathrm{sig}} \\ P_{\mathrm{sig}} \end{pmatrix}$$

$$= R\eta T A_{\mathrm{LO}} A_{\mathrm{sig}} \begin{pmatrix} \cos\left(\phi_{\mathrm{sig}} + \Delta\varphi_{\mathrm{slow}}\right) \\ \sin\left(\phi_{\mathrm{sig}} + \Delta\varphi_{\mathrm{slow}}\right) \end{pmatrix}, \tag{15}$$

where X'_{sig} and P'_{sig} are quadrature components after compensation of fast-drift phase. And the phase $\varphi_{\mathrm{slow}} = \varphi_{\mathrm{slow}}^{\mathrm{sig}} - \varphi_{\mathrm{slow}}^{\mathrm{ref}}$ remain almost constant during a short period. φ_{slow} drifts slowly with time; therefore, one can compensate for it by dynamic phase estimation in one block. We use a method of finding φ_{slow} by traversing all angle values from 0 to 360 and then estimating it according to the cross-correlation values, called phase searching algorithm [26]. In our experiment, we set a block of 10000 quantum signal pulses, and half of them were used to search the phase. It is worth observing that the data used to search the phase can also be employed for parameter estimation and final key calculation. Fig. 4(a) and (b) show data correlation of the measured quadrature components X and P between Alice and Bob after fast-drift and slow-drift phase compensation, which verifies the phase compensation method is also applicable in this scheme.

IV. System Performance Analysis and Discussion

Finally, we have experimentally demonstrated a pilot-sequential GMCS CV-QKD system with a local LO by following the above steps. And the parameters about system performance, including transmittance, excess noise, and secret key rate of practical implementation of this scheme could be calculated from parameter estimation [43], as be seen in Fig. 5. The "Times" on the x axes represents the number of blocks of experimental data during 8 hours. The repetition rate of our experiment is 5 MHz. The real repetition rate of the quantum signal is half of 5 MHz because the pilot pulse accompanies each quantum signal pulse. From Fig. 5, we know that the polarization loss caused by MPC is so significant that the value of the secret key rate fluctuated severely. What's worse, the polarization drift from the MPC is almost irreversible unless we regulate it again. The performance of the system has been significantly improved after

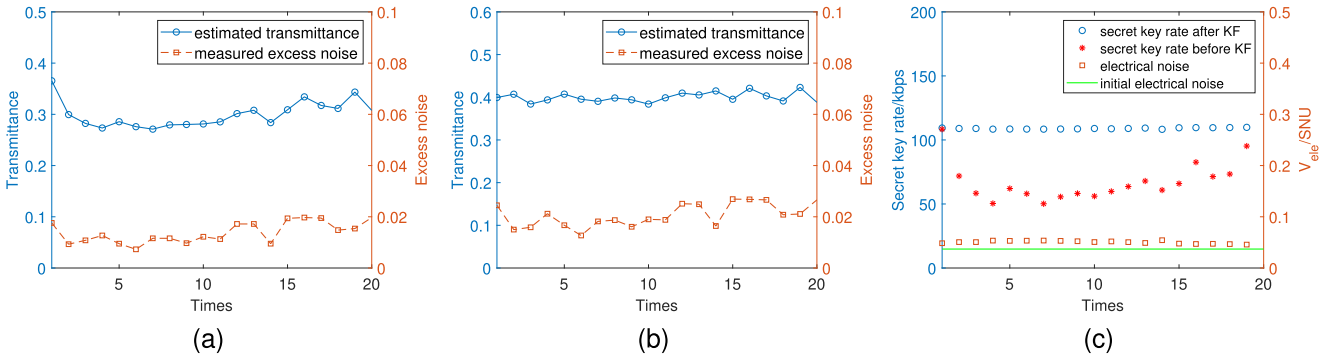

Fig. 5. (a) Transmittance and excess noise estimated before KF. (b) Transmittance and excess noise estimated after KF. (c) Secret key rate and electrical noise estimated before and after KF. The "initial electrical noise" is calibrated 0.037 SNU before the experiment and the "electrical noise" represents the electrical noise after polarization loss compensation. The modulation variance is 4.4139 SNU. The the reconciliation efficiency β is 0.95 [41]. Other parameters are calibrated as: the quantum efficiency η=0.48, the attenuation of fiber spool is 4 dB, the actual repetition is 2.5 MHz.

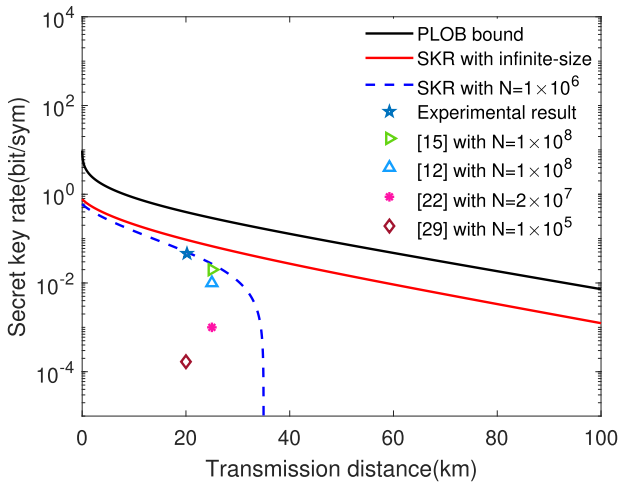

Fig. 6. Secure key rate versus transmission distance curves.The solid black line is the PLOB bound in this scheme [42]. The solid red line represent the calculated secure key rate (SKR) as a function of transmission distance in infinite-size scenarios. The blue dashed line denotes the secure key rate as a function of transmission distance under finite-size block of 1×10^6. The blue star represents the average value of experimental results. Other simulation parameters: the modulation variance is 4.4139 SNU, the quantum efficiency η=0.48, the reconciliation efficiency β is 0.95, the mean excess noise is 0.0206, the mean electrical noise is 0.0503 SNU.

using KF. On the one hand, based on the analysis in Appendix.B we obtain a low excess noise around 0.02. On the other hand, the KF algorithm can effectively control the transmittance of the system with around 0.4 which is the true transmittance under 20 km fiber with coefficient of 0.2 dB/km, and the secret key rate could reach 110 kbps as a relatively stable value under the finite-size block of 1×10^6. One imperfection is that the experimental data points after polarization loss compensation have some fluctuations. There are two main reasons: one is that the drift of the bias point from modulators cannot be completely avoided which would affect the modulation variance, the other is the statistical fluctuation in parameter estimation from the finite block size. It is noted that as the signal is amplified by KF, the corresponding excess noise and trusted electrical noise will also be strengthened, and this part of the noise can be calculated in this work, so the final total SNR remains unchanged. It can be seen that this work is important to maintain the long-term stable operation of the system when the SOP does not change drastically. Finally, the experimental and simulation results of the secret key rate corresponding to different transmission distances are shown in Fig. 6. The dark line is the PLOB bound of GMCS CV-QKD protocol with heterodyne detection. The solid red line represents the calculated secure key rate as a function of transmission distance in infinite-size scenarios. In contrast, the blue dashed line denotes the secret key rate as a function of transmission distance under the finite-size block of 1×10^6. It is worthy noting that the block size of 1×10^6 is optimal in this paper on condition of limited computing power from data recovery and post-processing and that is also a key reason why we choose 20 km as transmission distance in the experiment. The average secret key rate can reach around 0.044 b/sym under the transmission distance of 20 km. In addition, the previous experiment results are also shown in Fig. 6 for comparison, highlighting the proposed experimental scheme.

V. Conclusion

In conclusion, to achieve the long-term operation of the CV-QKD system, we use MPC interfered with KF algorithm to compensate the polarization loss in the laboratory where the SOP changes slowly. Besides, other DSP method including frequency estimation, orthogonal components acquiring, and phase compensation are explained and implemented to obtain final secret key rate in this paper. Finally, We have demonstrated a pilot-sequential GMCS CV-QKD system with a local LO completely. The experimental results show that the PLC method plays a crucial role in maintaining the stability of the secret key rate with high robustness. In other words, we can expect that this method can improve the system's robustness and a key rate of 110 kbps is achieved within 20 km optical fiber under the finite-size block of 1×10^6 during a more extended time according to the trend of the experimental results. It is worth noting that with the increase of the block data and repetition rate, the secret key rate would be further improved.

APPENDIX A
PRCCESS OF KF

The amplitude of the pilot signal is taken as the observation value, which is regarded as a classical signal. The measurement equation and the process equation of KF are given by [28]

$$U(k) = H(k)X(k) + V(k), \tag{16}$$

$$X(k) = A(k)X(k-1) + W(k), \tag{17}$$

where $U(k)$ represents the predicted polarization compensated signal, and $X(k)$ represents the state vector which should be estimated in the process. (16) and (17) are the measurement equation and the state transition equation while $V(k)$ and $W(k)$ are Gaussian noise function of above process respectively. The state X is the value of ${T_{\mathrm{P}}}^{-1}$ to be estimated in the process of Kalman filter while the transfer function H is exactly the calculated amplitude of the pilot signal. And $A(k)$ is the transfer coefficient of the state where $A(k) = 1$ in the model. According to the above model, the process of KF can be established as follows [29], [44]:

$$\begin{cases} X_{\mathrm{pre}}(k) = X(k-1) \\ P_{\mathrm{pre}}(k) = P(k-1) + Q \\ K(k) = P_{\mathrm{pre}}(k)H^T(k)\left[H(k)P_{\mathrm{pre}}(k)H^T(k) + R\right]^{-1} \\ X(k) = X_{\mathrm{pre}}(k) + K(k)[U_{\mathrm{o}}(k) - H(k)X_{\mathrm{pre}}(k)] \\ P(k) = [1 - K(k)H(k)]\,P_{\mathrm{pre}}(k) \end{cases} \tag{18}$$

where the first two formulas are time update equations while the remaining are measurement update equations. $X_{\mathrm{pre}}(k)$, $P_{\mathrm{pre}}(k)$, $K(k)$ and $P(k)$ are called the state prediction, priori estimate error covariance, Kalman gain and posteriori estimate error covariance, respectively. Q and R are noise variances of $W(k)$ and $V(k)$ which determines the estimation of the optimal value. $U_{\mathrm{o}}(k)$ is the observed data measured by us.

APPENDIX B
ANALYSIS OF EXCESS NOSIE

In CV-QKD, controlling the excess noise plays a vital role in achieving higher secret key rate of the system [16], [45]. Except for a fraction of noise, such as electrical noise ν_{el}, which can be regarded as trusted noise, other noises are treated as excess noise, which is controlled by Eve. In the LLO CV-QKD scheme, the excess noise can be expressed by [21]

$$\varepsilon_{\mathrm{tot}} = \varepsilon_{\mathrm{drift}} + \varepsilon_{\mathrm{channel}} + \varepsilon_{\mathrm{error}} + \varepsilon_{\mathrm{AM}} + \varepsilon_{\mathrm{Le}}, \tag{19}$$

where

$$\varepsilon_{\mathrm{drift}} = V_{\mathrm{A}} \cdot \left(2\pi\left(\Delta\nu_{\mathrm{A}} + \Delta\nu_{\mathrm{B}}\right)\Delta t\right). \tag{20}$$

The $\varepsilon_{\mathrm{drift}}$ presents the laser source drift noise resulting from laser phase drift between a time interval of Δt in this scheme, V_{A} is the modulation variance of the quantum state, and $\Delta\nu_{\mathrm{A}}$ and $\Delta\nu_{\mathrm{B}}$ denote the linewidth of two independent lasers at Alice and Bob, respectively. This paper defines this drift phase as φ_{slow} and can be compensated directly in Section III-D.

The $\varepsilon_{\mathrm{channel}}$ is defined as propagation phase drift noise by the following equation:

$$\varepsilon_{\mathrm{channel}} = V_{\mathrm{A}} \cdot \mathrm{var}\left(\varphi_{\mathrm{channel}}^{\mathrm{sig}} - \varphi_{\mathrm{channel}}^{\mathrm{ref}}\right), \tag{21}$$

which is induced from the relative phase drift accumulated by the quantum signal and pilot signal during propagation. In this scheme, the two kinds of signals follow the same optical path, so the $\varepsilon_{\mathrm{channel}} \approx 0$ can also be interpreted in Section III-A.

The phase estimation error noise $\varepsilon_{\mathrm{error}}$ originates from the pilot pulse quantum uncertainty at the detector as a result of the shot noise and total noise χ_{tot} of the system, which describes the error between the ideal phase and the calculated phase of the pilot signal. The value is inversely proportional to the intensity of the pilot signal, expressed as

$$\varepsilon_{\mathrm{error}} = V_{\mathrm{A}} \cdot \left(\frac{\chi_{\mathrm{tot}} + 1}{(E_{\mathrm{R}})^2}\right), \tag{22}$$

where E_{R} is the amplitude of the pilot pulse, we can quantitatively understand from (14) that increasing the amplitude E_{R} can reduce the contribution of the $\varepsilon_{\mathrm{error}}$, which corresponds to why we employ the second AM to enhance the accuracy of phase compensation mentioned in Section II. In addition, the above three noises are from phase compensation, called phase noise, and are independent of each other.

The interleaved intense pilot pulse and the weak quantum signal are generated using a single amplitude modulator in the pilot-sequential LLO CV-QKD system. However, in practice, the efficiency of the amplitude modulator is limited by its finite dynamic range, which restricts the pilot pulse's maximum amplitude, which would introduce a leakage on the quantum signal. The dynamic range d_{dB} characterizes the relationship between the maximum amplitude E_{max} and minimum amplitude E_{min}, defined as [21]

$$d_{\mathrm{dB}} = 10\log_{10}\left(\frac{E_{\mathrm{max}}^2}{E_{\mathrm{min}}^2}\right), \tag{23}$$

which is also defined as the extinction ratio of the amplitude modulator. The leakage on the weak quantum signal would introduce additional noise $\varepsilon_{\mathrm{AM}}$ which can be written as

$$\varepsilon_{\mathrm{AM}} = E_{\mathrm{R}}^2 \cdot 10^{-d_{\mathrm{dB}}/10}. \tag{24}$$

From the above equation, two methods are shown to be available in reducing the noise: one is decreasing the amplitude of the pilot pulse, which is contradicted against (14); the other way is to increase the extinction ratio of the AM. Considering this, it is the second reason why we employ the second AM to increase the extinction ratio from two cascaded amplitude modulators. In this way, the extinction ratio can be got 70 dB while the $\varepsilon_{\mathrm{AM}} << 0.01$ and can be ignored approximately.

Finally, the photon leakage noise $\varepsilon_{\mathrm{Le}}$ result from the photon leakage from the pilot pulses to the quantum signals in the pilot-multiplexed scheme and $\varepsilon_{\mathrm{Le}} \approx 0$ in this scheme. It is worth noting that the most excess noise can be suppressed as much as possible, and this scheme is also an advantage.

APPENDIX C
SECRET KEY RATE UNDER FINITE-SIZE EFFECT

In this section, the asymptotic secret key rate of GMCS LLO-CVQKD with heterodyne detection is conducted for simplicity, and we only show the secret key rate for reverse reconciliation [11], [23]:

$$K = f \cdot \frac{n}{N} \left(\beta I_{\mathrm{AB}} - \chi_{\mathrm{BE}},\right) \tag{25}$$

where f is the repetition frequency of the quantum signal. N represents the total number of a block while n represents the number for key calculation. The β is the reconciliation efficiency, I_{AB} is the mutual information between Alice and Bob, χ_{BE} is the maximum information available to Eve on Bob's key, which is bounded by Holevo quantity. And I_{AB} can be derived from the Shannon equation as

$$I_{\mathrm{AB}} = \log_2 \frac{V_{\mathrm{A}} + 1 + \chi_{\mathrm{tot}}}{1 + \chi_{\mathrm{tot}}}, \tag{26}$$

where χ_{tot} represents the noise referred to channel input and can be calculated as $\chi_{\mathrm{tot}} = \chi_{\mathrm{line}} + \chi_{\mathrm{het}}/T$, where $\chi_{\mathrm{line}} = 1/T - 1 + \varepsilon$, and $\chi_{\mathrm{het}} = [1 + (1-\eta) + 2\upsilon_{\mathrm{el}}]/\eta$. The mutual information between Bob and Eve is given by

$$\chi_{\mathrm{BE}} = \sum_{i=1}^{2} G\left(\frac{\lambda_i - 1}{2}\right) + \sum_{i=3}^{5} G\left(\frac{\lambda_i - 1}{2}\right), \tag{27}$$

where $G(x) = (x+1)\log_2(x+1) - x\log_2 x$, and λ_i are symplectic eigenvalues and can be calculated as [46]

$$\begin{aligned} \lambda_{1,2}^2 &= \frac{1}{2}\left(A \pm \sqrt{A^2 - 4B}\right), \\ \lambda_{3,4}^2 &= \frac{1}{2}\left(C \pm \sqrt{C^2 - 4D}\right), \\ \lambda_5 &= 1, \end{aligned} \tag{28}$$

where

$$\begin{aligned} A &= V^2(1 - 2\,T) + 2T + T^2\left(V + \chi_{\mathrm{line}}\right)^2, \\ B &= \left[T\left(V\chi_{\mathrm{line}} + 1\right)\right]^2, \\ C &= \frac{1}{\left(T\left(V + \chi_{\mathrm{tot}}\right)\right)^2}\left[A\chi_{\mathrm{het}}^2 + B + 1\right. \\ &\quad \left. + 2\chi_{\mathrm{het}}\left(V\sqrt{B} + T\left(V + \chi_{\mathrm{line}}\right)\right) + 2T\left(V^2 - 1\right)\right], \\ D &= \left(\frac{V + \sqrt{B}\chi_{\mathrm{het}}}{T\left(V + \chi_{\mathrm{tot}}\right)}\right)^2. \end{aligned} \tag{29}$$

In the case of finite-size effect, the transmittance T would get a lower bound while the excess noise ε would reach a upper bound, written as [47]

$$\begin{aligned} T_{\min} &= \frac{\left(\sqrt{\eta T} - \Delta T\right)^2}{\eta}, \\ \varepsilon_{\max} &= \varepsilon + \frac{\Delta\sigma_0^2}{\eta T}, \end{aligned} \tag{30}$$

where

$$\begin{aligned} \Delta T &= \zeta_{\delta_{\mathrm{PE}}/2}\sqrt{\frac{\sigma^2}{m V_{\mathrm{A}}}}, \\ \Delta\sigma_0^2 &= \zeta_{\delta_{\mathrm{PE}}/2}\frac{\sigma^2\sqrt{2}}{\sqrt{m}}, \end{aligned} \tag{31}$$

where $\zeta_{\delta_{\mathrm{PE}}/2}$ is the confidence coefficient, $\sigma^2 = \eta T\varepsilon + 1 + \upsilon_{el}$, and $m = N - n$ is the number of the signal pulse for parameter estimation.

REFERENCES

[1] F. Xu, X. Ma, Q. Zhang, H.-K. Lo, and J.-W. Pan, "Secure quantum key distribution with realistic devices," *Rev. Modern Phys.*, vol. 92, no. 2, 2020, Art. no. 025002.

[2] S. Pirandola et al., "Advances in quantum cryptography," *Adv. Opt. Photon.*, vol. 12, no. 4, pp. 1012–1236, 2020.

[3] R. García-Patrón and N. J. Cerf, "Unconditional optimality of Gaussian attacks against continuous-variable quantum key distribution," *Phys. Rev. Lett.*, vol. 97, no. 19, 2006, Art. no. 190503.

[4] M. Navascués, F. Grosshans, and A. Acin, "Optimality of Gaussian attacks in continuous-variable quantum cryptography," *Phys. Rev. Lett.*, vol. 97, no. 19, 2006, Art. no. 190502.

[5] S. Pirandola, S. L. Braunstein, and S. Lloyd, "Characterization of collective Gaussian attacks and security of coherent-state quantum cryptography," *Phys. Rev. Lett.*, vol. 101, no. 20, 2008, Art. no. 200504.

[6] R. Renner and J. I. Cirac, "de finetti representation theorem for infinite-dimensional quantum systems and applications to quantum cryptography," *Phys. Rev. Lett.*, vol. 102, no. 11, 2009, Art. no. 110504.

[7] A. Leverrier, R. García-Patrón, R. Renner, and N. J. Cerf, "Security of continuous-variable quantum key distribution against general attacks," *Phys. Rev. Lett.*, vol. 110, no. 3, 2013, Art. no. 030502.

[8] F. Furrer et al., "Continuous variable quantum key distribution: Finite-key analysis of composable security against coherent attacks," *Phys. Rev. Lett.*, vol. 109, no. 10, 2012, Art. no. 100502.

[9] A. Leverrier, "Composable security proof for continuous-variable quantum key distribution with coherent states," *Phys. Rev. Lett.*, vol. 114, no. 7, 2015, Art. no. 070501.

[10] S. Pirandola, "Composable security for continuous variable quantum key distribution: Trust levels and practical key rates in wired and wireless networks," *Phys. Rev. Res.*, vol. 3, no. 4, 2021, Art. no. 043014.

[11] F. Grosshans, G. Van Assche, J. Wenger, R. Brouri, N. J. Cerf, and P. Grangier, "Quantum key distribution using Gaussian-modulated coherent states," *Nature*, vol. 421, no. 6920, pp. 238–241, 2003.

[12] P. Jouguet, S. Kunz-Jacques, A. Leverrier, P. Grangier, and E. Diamanti, "Experimental demonstration of long-distance continuous-variable quantum key distribution," *Nature Photon.*, vol. 7, no. 5, pp. 378–381, 2013.

[13] Y. Huang et al., "Realizing a downstream-access network using continuous-variable quantum key distribution," *Phys. Rev. Appl.*, vol. 16, no. 6, 2021, Art. no. 064051.

[14] D. Milovančev, N. Vokić, F. Laudenbach, C. Pacher, H. Hübel, and B. Schrenk, "High rate CV-QKD secured mobile WDM fronthaul for dense 5G radio networks," *J. Lightw. Technol.*, vol. 39, no. 11, pp. 3445–3457, Jun. 2021.

[15] D. Huang et al., "Continuous-variable quantum key distribution with 1 mbps secure key rate," *Opt. Exp.*, vol. 23, no. 13, pp. 17511–17519, 2015.

[16] D. Huang, P. Huang, D. Lin, and G. Zeng, "Long-distance continuous-variable quantum key distribution by controlling excess noise," *Sci. Rep.*, vol. 6, no. 1, pp. 1–9, 2016.

[17] Y. Zhang et al., "Continuous-variable QKD over 50 km commercial fiber," *Quantum Sci. Technol.*, vol. 4, no. 3, 2019, Art. no. 035006.

[18] Y. Zhang et al., "Long-distance continuous-variable quantum key distribution over 202.81 km of fiber," *Phys. Rev. Lett.*, vol. 125, no. 1, 2020, Art. no. 010502.

[19] H. Wang et al., "Sub-Gbps key rate four-state continuous-variable quantum key distribution within metropolitan area," *Commun. Phys.*, vol. 5, no. 1, pp. 1–10, 2022.

[20] Y. Tian et al., "Experimental demonstration of continuous-variable measurement-device-independent quantum key distribution over optical fiber," *Optica*, vol. 9, no. 5, pp. 492–500, 2022.

[21] A. Marie and R. Alleaume, "Self-coherent phase reference sharing for continuous-variable quantum key distribution," *Phys. Rev. A*, vol. 95, no. 1, 2017, Art. no. 012316.

[22] D. Huang, P. Huang, D. Lin, C. Wang, and G. Zeng, "High-speed continuous-variable quantum key distribution without sending a local oscillator," *Opt. Lett.*, vol. 40, no. 16, pp. 3695–3698, 2015.

[23] T. Wang, P. Huang, Y. Zhou, W. Liu, and G. Zeng, "Pilot-multiplexed continuous-variable quantum key distribution with a real local oscillator," *Phys. Rev. A*, vol. 97, no. 1, 2018, Art. no. 012310.

[24] H. Wang et al., "High-speed gaussian-modulated continuous-variable quantum key distribution with a local local oscillator based on pilot-tone-assisted phase compensation," *Opt. Exp.*, vol. 28, no. 22, pp. 32882–32893, 2020.

[25] B. Qi, P. Lougovski, R. Pooser, W. Grice, and M. Bobrek, "Generating the local oscillator "locally" in continuous-variable quantum key distribution based on coherent detection," *Phys. Rev. X*, vol. 5, no. 4, 2015, Art. no. 041009.

[26] T. Wang et al., "High key rate continuous-variable quantum key distribution with a real local oscillator," *Opt. Exp.*, vol. 26, no. 3, pp. 2794–2806, 2018.

[27] T. Shen, Y. Huang, X. Wang, H. Tian, Z. Chen, and S. Yu, "Strengthening practical continuous-variable quantum key distribution against measurement angular error," *Opt. Exp.*, vol. 29, no. 20, pp. 30978–30990, 2021.

[28] Y. Yang et al., "Fast polarization-state tracking scheme based on radius-directed linear Kalman filter," *Opt. Exp.*, vol. 23, no. 15, pp. 19673–19680, 2015.

[29] T. Wang, P. Huang, S. Wang, and G. Zeng, "Polarization-state tracking based on Kalman filter in continuous-variable quantum key distribution," *Opt. Exp.*, vol. 27, no. 19, pp. 26689–26700, 2019.

[30] B. Huang, Y. Huang, and Z. Peng, "Tracking reference phase with a Kalman filter in continuous-variable quantum key distribution," *Opt. Exp.*, vol. 28, no. 19, pp. 28727–28739, 2020.

[31] H.-M. Chin, N. Jain, D. Zibar, U. L. Andersen, and T. Gehring, "Machine learning aided carrier recovery in continuous-variable quantum key distribution," *Npj Quantum Inf.*, vol. 7, no. 1, pp. 1–6, 2021.

[32] X. Wang, H. Wang, C. Zhou, Z. Chen, S. Yu, and H. Guo, "Continuous-variable quantum key distribution with low-complexity information reconciliation," *Opt. Exp.*, vol. 30, no. 17, pp. 30455–30465, 2022.

[33] X. Wang, Y. Zhang, S. Yu, and H. Guo, "High-speed implementation of length-compatible privacy amplification in continuous-variable quantum key distribution," *IEEE Photon. J.*, vol. 10, no. 3, pp. 1–9, Jun. 2018.

[34] B.-Z. Yan, Q. Li, H.-K. Mao, H.-W. Xu, and A. A. Abd El-Latif, "Large-scale and high-speed fpga-based privacy amplification for quantum key distribution," *J. Lightw. Technol.*, vol. 41, no. 1, pp. 169–175, Jan. 2023.

[35] W. Zhao, Y. Guo, L. Zhang, and D. Huang, "Phase noise estimation using Bayesian inference for continuous-variable quantum key distribution," *Opt. Exp.*, vol. 27, no. 3, pp. 1838–1853, 2019.

[36] T. Wang, P. Huang, S. Wang, and G. Zeng, "Carrier-phase estimation for simultaneous quantum key distribution and classical communication using a real local oscillator," *Phys. Rev. A*, vol. 99, no. 2, 2019, Art. no. 022318.

[37] Z. Chen, X. Wang, S. Yu, Z. Li, and H. Guo, "Digital continuous-variable quantum key distribution," 2022, *arXiv:2207.04991*.

[38] W. Liu, X. Wang, N. Wang, S. Du, and Y. Li, "Imperfect state preparation in continuous-variable quantum key distribution," *Phys. Rev. A*, vol. 96, no. 4, 2017, Art. no. 042312.

[39] R. Corvaja, "Phase-noise limitations in continuous-variable quantum key distribution with homodyne detection," *Phys. Rev. A*, vol. 95, no. 2, 2017, Art. no. 022315.

[40] D. B. Soh et al., "Self-referenced continuous-variable quantum key distribution protocol," *Phys. Rev. X*, vol. 5, no. 4, 2015, Art. no. 041010.

[41] X. Wang, Y. Zhang, S. Yu, B. Xu, Z. Li, and H. Guo, "Efficient rate-adaptive reconciliation for continuous-variable quantum key distribution," *Quantum Inf. Computation*, vol. 17, no. 13–14, pp. 1123–1134, 2017.

[42] S. Pirandola, R. Laurenza, C. Ottaviani, and L. Banchi, "Fundamental limits of repeaterless quantum communications," *Nature Commun.*, vol. 8, no. 1, pp. 1–15, 2017.

[43] Z. Chen, Y. Zhang, X. Wang, S. Yu, and H. Guo, "Improving parameter estimation of entropic uncertainty relation in continuous-variable quantum key distribution," *Entropy*, vol. 21, no. 7, 2019, Art. no. 652.

[44] G. Welch and G. Bishop, "An introduction to the Kalman filter," in *Proc. SIGGRAPH Course*, 2001, vol. 8, p. 41.

[45] J. Lodewyck, T. Debuisschert, R. Tualle-Brouri, and P. Grangier, "Controlling excess noise in fiber-optics continuous-variable quantum key distribution," *Phys. Rev. A*, vol. 72, no. 5, 2005, Art. no. 050303.

[46] S. Fossier, E. Diamanti, T. Debuisschert, R. Tualle-Brouri, and P. Grangier, "Improvement of continuous-variable quantum key distribution systems by using optical preamplifiers," *J. Phys. B: Atomic, Mol. Opt. Phys.*, vol. 42, no. 11, 2009, Art. no. 114014.

[47] A. Leverrier, F. Grosshans, and P. Grangier, "Finite-size analysis of a continuous-variable quantum key distribution," *Phys. Rev. A*, vol. 81, no. 6, 2010, Art. no. 062343.